Chapter 7
On the Flow Through Bering Strait: A Synthesis of Model Results and Observations

Jaclyn Clement Kinney, Wieslaw Maslowski, Yevgeny Aksenov, Beverly de Cuevas, Jaromir Jakacki, An Nguyen, Robert Osinski, Michael Steele, Rebecca A. Woodgate, and Jinlun Zhang

Abstract Bering Strait is the only ocean connection between the Pacific and the Arctic. The flow through this narrow and shallow strait links the Pacific and Arctic oceans and impacts oceanic conditions downstream in the Chukchi Sea and the Western Arctic. We present a model synthesis of exchanges through Bering Strait at monthly to decadal time scales, including results from coupled ice-ocean models and observations. Significant quantities of heat and freshwater are delivered annually into the southern Chukchi Sea via Bering Strait. We quantify seasonal signals, along with interannual variability, over the course of 26 years of multiple model integrations. Volume transport and property fluxes are evaluated among several high-resolution model runs and compared with available moored observations. High-resolution models represent the bathymetry better, and may have a more realistic representation of the flow through the strait, although in terms of fluxes and mean properties, this is not always the case. We conclude that, (i) while some of the models used for Arctic studies achieve the correct order of magnitude for fluxes of volume, heat and freshwater, and have significant correlations with observational results, there is still a need for improvement and (ii) higher spatial

J. Clement Kinney (✉) • W. Maslowski
Department of Oceanography, Graduate School of Engineering and Applied Sciences, Naval Postgraduate School, Dyer Road, Bldg. SP339B, Monterey, CA 93943, USA
e-mail: jlclemen@nps.edu; maslowsk@nps.edu

Y. Aksenov • B. de Cuevas
Marine Systems Modelling, National Oceanography Centre, Southampton, UK

J. Jakacki • R. Osinski
Institute of Oceanology, Polish Academy of Sciences, Powstancow Warszawy 55, Sopot 81-712, Poland

A. Nguyen
Program in Atmospheres, Oceans, and Climate, Massachusetts Institute of Technology, Cambridge, MA, USA

M. Steele • R.A. Woodgate • J. Zhang
Applied Physics Laboratory, University of Washington, Seattle, WA, USA

J.M. Grebmeier and W. Maslowski (eds.), *The Pacific Arctic Region: Ecosystem Status and Trends in a Rapidly Changing Environment*, DOI 10.1007/978-94-017-8863-2_7,

resolution is needed to resolve features such as the Alaska Coastal Current (ACC). At the same time, additional measurements with better spatial coverage are needed to minimize uncertainties in observed estimates and to constrain models.

Keywords Bering Strait • Ocean modeling • Pacific water • Numerical modeling

7.1 Introduction

The Pacific Arctic Region spans the sub-Arctic Bering Sea northward through the Chukchi and Beaufort seas and the Arctic Ocean. The Bering Strait, a narrow passageway, connects the wide and shallow shelves of the Bering and Chukchi seas and is the only Pacific connection to the Arctic Ocean. The narrow (~85 km wide) and shallow (~50 m deep) strait provides low-salinity and high-nutrient Pacific Water to the Chukchi Sea and the Arctic Ocean. Many global and regional models face challenges with resolving oceanic exchanges across this narrow and shallow strait, mainly due to the requirement of high spatial resolution and the associated high computational cost to resolve it. In fact, many coarse-resolution models either have a closed Bering Strait or use a prescribed boundary condition. However, Goosse et al. (1997) demonstrated that there is a significant improvement in modeled ocean dynamics in a coarse resolution ($3° \times 3°$) model with an opened Bering Strait. They also found that opening Bering Strait produced a more realistically positioned sea ice edge in the Bering Sea, because warm water was allowed to advect further north onto the Bering-Chukchi shelf. Arctic freshwater budgets were also improved, with increased freshwater storage in the Greenland and Norwegian Seas.

Scientific access across Bering Strait has been restricted due to the political boundary between the United States and Russia. The Russian-US Convention line, dividing the Exclusive Economic Zones (EEZs) of the two countries, lies between two islands near the center of the strait: Ratmanova Island (part of Russia, also called Big Diomede in the U.S.) and Little Diomede Island (part of the U.S.). While U.S. research has maintained moorings in the Bering Strait almost continuously since 1990, only for limited portions of that time has U.S. access been granted to the western side of the strait.

The first goal of this work is to compare state-of-the-art output on the Bering Strait throughflow from several regional and global Arctic-focused models. We will analyze the volume and property fluxes over a long time series (up to 26 years depending on available results from individual models). In addition to interannual changes, we will also examine seasonal cycles in these parameters. The second related goal of this work is to compare model results with the available observational data. These data are from moored instruments placed near-bottom in three point locations in the vicinity of the strait (Fig. 7.1a). Both observations and models have their own limitations in Bering Strait. Numerical models are limited by relatively coarse resolution in the strait, errors in forcing and omitted processes

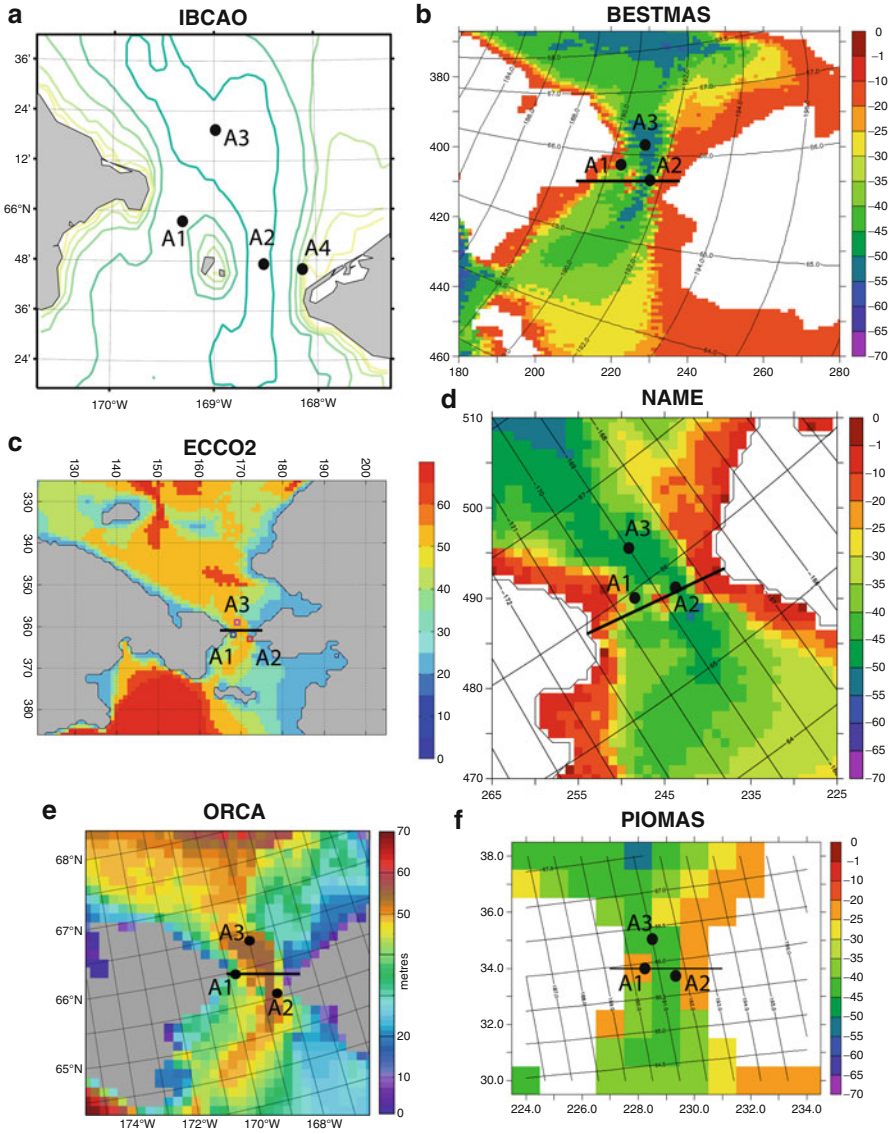

Fig. 7.1 Bathymetry (m) in the vicinity of the Bering Strait (**a**). Depth contours are every 10 m from the International Bathymetric Chart of the Arctic Ocean (Jakobsson et al. 2000). Model bathymetry (m) from (**b**) BESTMAS, (**c**) ECCO2, (**d**) NAME, (**e**) ORCA, and (**f**) PIOMAS. The approximate locations of the moored observations are indicated with *black circles*. The cross-sections across Bering Strait are shown as *black lines* in each model bathymetry figure

(e.g., tides), whereas observational results are limited by spatial coverage across the strait, and lack of upper layer measurements.

7.2 Model Descriptions

In this section we describe five global and regional sea ice-ocean coupled models employed to investigate Bering Strait inflow (Table 7.1). The models used in the study have various design features, including resolution, atmospheric forcing, restoring terms, coefficients, and parameterizations. Details of these features for each model are discussed below and shown in Tables 7.1 and 7.2. The goal here is to present results on the flow through Bering Strait from a variety of models and assess differences among them and observed data.

7.2.1 Bering Ecosystem Study Ice-Ocean Modeling and Assimilation System (BESTMAS)

BESTMAS (Zhang et al. 2010) is based on the coupled Parallel Ocean and sea Ice Model (POIM) of Zhang and Rothrock (2003). The sea ice model is the multicategory thickness and enthalpy distribution (TED) sea ice model (Zhang and Rothrock 2001; Hibler 1980). It employs a teardrop viscous-plastic rheology (Zhang and Rothrock 2005), a mechanical redistribution function for ice ridging (Thorndike et al. 1975; Hibler 1980), and a LSR (line successive relaxation) dynamics model to solve the ice momentum equation (Zhang and Hibler 1997). The TED ice model also includes a snow thickness distribution model following Flato and Hibler (1995). The ocean model is based on the Parallel Ocean Program (POP) developed at Los Alamos National Laboratory (Smith et al. 1992; Dukowicz and Smith 1994). Given that tidal energy accounts for 60–90 % of the total horizontal kinetic energy over the southeastern shelf region of the Bering Sea (Kinder and Schumacher 1981), tidal forcing arising from the eight primary constituents (M2, S2, N2, K2, K1, O1, P1, and Q1) (Gill 1982) is incorporated into the POP ocean model. The tidal forcing

Table 7.1 Basic information on the five models used in this study

Model	Global/regional	Atmospheric forcing	Resolution in Bering Strait	Data assimilation?
BESTMAS	Regional	NCEP/NCAR reanalysis	~4 km	No
ECCO2	Regional	Japanese 25-year reanalysis	~23 km	No
NAME	Regional	ECMWF reanalysis	~9 km	No
ORCA	Global	DRAKKAR Forcing Set (DFS 3.1) reanalysis	~13 km	No
PIOMAS	Regional	NCEP/NCAR reanalysis	~40 km	No

Table 7.2 Cross-sectional area across Bering Strait for the models and observations and friction coefficients for the models

Model/ observed	Area (km^2)	Bottom friction coefficient	Lateral boundary condition	Lateral friction coefficient	Surface friction coefficient	
					Ice-Ocean	Air-Ocean
BESTMAS	3.24	Quadratic bottom drag: 1.225×10^{-3}	No-slip	Variable momentum harmonic horizontal mixing depending on variable grid size	5.5×10^{-3}	1.0×10^{-3}
ECCO2	4.50	Quadratic bottom drag: 2.1×10^{-3}	Free-slip	Modified Leith [Fox-Kemper and Menemenlis 2008]	5.4×10^{-3}	Large and Pond (1981, 1982)
NAME	2.37	Quadratic bottom drag: 1.225×10^{-3}	No-slip	Momentum biharmonic horizontal mixing: -1.25×10^{18}	5.5×10^{-3}	0.6×10^{-3}
Observed	2.60	N/A	N/A	N/A	N/A	N/A
ORCA	4.17	Quadratic bottom drag: 1.0×10^{-3}	Free-slip	Bi-harmonic (−1.5e+11 m4/s)	Quadratic, 5.0×10^{-3}	CORE bulk formulae, Large and Yeager (2004)
PIOMAS	2.38	Quadratic bottom drag: 1.225×10^{-3}	No-slip	Variable momentum harmonic horizontal mixing depending on variable grid size	5.5×10^{-3}	1.0×10^{-3}

consists of a tide generating potential with corrections due to both the earth tide and self-attraction and loading following Marchuk and Kagan (1989). The model domain of BESTMAS covers the northern hemisphere north of 39°N. The BESTMAS finite-difference grid is based on a generalized orthogonal curvilinear coordinate system with a horizontal dimension of 600 × 300 grid points. The "north pole" of the model grid is placed in Alaska. Thus, BESTMAS has its highest horizontal resolution along the Alaskan coast and in the Bering, Chukchi, and Beaufort seas, with an average of about 7 km for the whole Bering Sea and 10 km for the combined Chukchi and Beaufort seas. There are 26 grid cells across Bering Strait (Fig. 7.1b), which allows a good connection between the Bering Sea and the Arctic Ocean. The TED sea ice model has eight categories each for ice thickness, ice enthalpy, and snow depth. The centers of the 8 ice thickness categories are 0, 0.38, 1.30, 3.07, 5.97, 10.24, 16.02, and 23.41 m. The POP ocean model has 30 vertical levels of varying thicknesses to resolve surface layers and bottom topography. The first 13 levels are in the upper 100 m and the upper six levels are each 5 m thick. The model bathymetry is obtained by merging the IBCAO (International Bathymetric Chart of the Arctic Ocean) dataset and the ETOPO5 (Earth Topography Five Minute Gridded Elevation Data Set) dataset (see Holland 2000). BESTMAS is forced by daily NCEP/NCAR reanalysis (Kalnay et al. 1996) surface forcing fields. Model forcing also includes river runoff of freshwater in the Bering and Arctic seas. For the Bering Sea, monthly climatological runoffs of the Anadyr, Yukon, and Kuskokwim rivers are used (Zhang et al. 2010). For the Arctic Ocean, monthly climatological runoffs of the Pechora, Ob, Yenisei, Olenek, Yana, Indigirka, Kolyma, Mackenzie, Dvina, Lena, Khatanga, Taimyra, and Piasina rivers are from the Alfred Wegener Institute (Prange and Lohmann 2004). Although BESTMAS has a large model domain that includes the Arctic and the North Pacific, realistic lateral open boundary conditions are still necessary to create the right water masses and fluxes. The POP ocean model has been further modified to incorporate open boundary conditions so that BESTMAS is able to be one-way nested to a lower resolution but global POIM (Zhang 2005). Monthly mean open boundary conditions of ocean temperature, salinity, and sea surface height from the global POIM are imposed at the southern boundaries along 39°N. No data were assimilated in BESTMAS.

7.2.2 Estimating the Circulation and Climate of the Ocean, Phase II (ECCO2)

The ECCO2 regional Arctic Ocean solution uses a configuration of the Massachusetts Institute of Technology general circulation model (MITgcm; Marshall et al. 1997; Losch et al. 2010; Nguyen et al. 2011). The domain boundaries are at ~55° North in both the Atlantic and Pacific sectors. These boundaries coincide with grid cells in a global, cubed-sphere configuration of the MITgcm (Menemenlis et al. 2005).

The grid covering the Arctic domain is locally orthogonal with horizontal grid spacing of approximately 18 km. There are 50 vertical levels ranging in thickness

from 10 m near the surface to approximately 450 m at a maximum model depth of 6,150 m. The model employs the rescaled vertical coordinate "z*" of Adcroft and Campin (2004) and the partial-cell formulation of Adcroft et al. (1997), which permits accurate representation of the bathymetry. Bathymetry is from the S2004 (W. Smith, 2010, personal communication) blend of the Smith and Sandwell (1997) and the General Bathymetric Charts of the Oceans (GEBCO) one arc-minute bathymetric grid. The non-linear equation of state of Jackett and McDougall (1995) is used. Vertical mixing follows Large et al. (1994). A 7th-order monotonicity-preserving advection scheme of Daru and Tenaud (2004) is employed and there is no explicit horizontal diffusivity. Horizontal viscosity follows Leith (1996) but is modified to sense the divergent flow (Fox-Kemper and Menemenlis 2008).

The ocean model is coupled to the MITgcm sea ice model described in Losch et al. (2010). Ice mechanics follow a viscous-plastic rheology and the ice momentum equations are solved numerically using the line-successive-over-relaxation (LSOR) solver of Zhang and Hibler (1997). Ice thermodynamics use a zero-heat-capacity formulation and seven thickness categories, equally distributed between zero to twice the mean ice thickness in each grid cell. Ice dynamics use a 2-category thickness with one for open water and one for ice. Salt rejected during ice formation is treated using a sub-grid-scale salt-plume parameterization described in Nguyen et al. (2009). The model includes prognostic variables for snow thickness and for sea ice salinity.

Initial and lateral boundary conditions come from the globally optimized ECCO2 solution (Menemenlis et al. 2008). Surface atmospheric forcing fields are from the Japanese 25-year reanalysis (JRA25; Onogi et al. 2007). Monthly mean river runoff is based on the Arctic Runoff Data Base (ARDB) as prepared by P. Winsor (2007, personal communication). No restoring is used.

Ocean and sea ice parameters, such as mixing and drag coefficients and albedos, were optimized regionally based on observations (Nguyen et al. 2011). The model results presented here are from a 1992 to 2008 forward model run using the optimized parameters and do not assimilate any data. The model bathymetry in the vicinity of Bering Strait and the location of the Bering Strait cross-section are shown in Fig. 7.1c. The mean horizontal grid spacing of the model across Bering Strait is 23 km.

7.2.3 Naval Postgraduate School Arctic Modeling Effort (NAME)

The NAME coupled sea-ice–ocean model (Maslowski et al. 2004) has a horizontal grid spacing of 1/12° (or ~9 km). In the vertical direction, there are 45 vertical depth layers ranging from 5 m near the surface to 300 m at depth, with eight levels in the upper 50 m. The high vertical resolution, especially in the upper water column, allows for more realistic representation of the shallow Arctic and sub-Arctic shelves. In addition, the horizontal grid permits calculation of flow through the narrow straits

of the northern Bering Sea (Clement et al. 2005). The model domain is configured in a rotated spherical coordinate system to minimize changes in grid cell area. It contains the sub-Arctic North Pacific (including the Sea of Japan and the Sea of Okhotsk) and North Atlantic Oceans, the Arctic Ocean, the Canadian Arctic Archipelago (CAA) and the Nordic Seas (see Fig. 7.1a of Maslowski et al. 2004 for model domain). The region of interest, the Bering Sea, is therefore far away from the artificially closed lateral boundaries in the North Pacific at 30°N, greatly reducing any potential effects of boundary conditions. In an effort to balance the net flow of Pacific Ocean water into the Arctic Ocean, a U-shaped 500 m deep, 162 km (18 grid point) wide channel was created through North America connecting the Atlantic Ocean to the Pacific Ocean. A westward wind forcing of 1.75 dyne cm^{-2} is prescribed along the channel (see Maslowski et al. 2004 for further details). Flow through the Bering Strait and the channel is not prescribed. There are 15 grid cells across Bering Strait in this model (Fig. 7.1d). Model bathymetry is derived from two sources: ETOPO5 at 5 km resolution for the region south of 64°N and International Bathymetric Chart of the Arctic Ocean (IBCAO; Jakobsson et al. 2000) at 2.5 km resolution for the region north of 64°N.

The ocean model was initialized with climatological, 3-dimensional temperature and salinity fields (PHC; Steele et al. 2001) and integrated for 48 years in a spinup mode. During the spinup, daily averaged annual climatological atmospheric forcing derived from 1979 to 1993 reanalysis from the European Centre for Medium-Range Weather Forecasts (ECMWF) was used for 27 years. Next an additional run was performed using repeated 1979 ECMWF annual cycle for 6 years and then 1979–1981 interannual fields for the last 15 years of the 48-year spinup. This approach is especially important in establishing realistic ocean circulation representative of the time period at the beginning of the actual interannual integration. This final run with realistic daily averaged ECMWF interannual forcing starts in 1979 and continues through 2004. Results from this integration (26 years) are used for the analyses in this chapter. Daily climatological runoff from the Yukon River (and all other major Arctic rivers) is included in the model as a virtual freshwater flux at the river mouth. However, in the Gulf of Alaska the freshwater flux from runoff (Royer 1981) is introduced by restoring the surface ocean level (of 5 m) to climatological (Polar Science Center Hydrographic Climatology; PHC) monthly mean temperature and salinity values over a monthly time scale (as a correction term to the explicitly calculated fluxes between the ocean and underlying atmosphere or sea-ice). Additional details on the model including sea-ice and river runoff have been provided elsewhere (Maslowski et al. 2004).

7.2.4 Nucleus for European Modelling of the Ocean (NEMO) with ORCA Configuration

The ORCA025-N102 model configuration of the National Oceanography Centre Southampton is an “eddy-permitting” z-level global coupled sea ice-ocean model. ORCA025-N102 was developed within the Nucleus for European Modelling of the

Ocean (NEMO) framework for ocean climate research and operational oceanography (http://www.nemo-ocean.eu/; Madec 2008) as part of the DRAKKAR configurations (DRAKKAR Group 2007) and is largely based on the ORCA025-G70 configuration (e.g., Lique et al. 2009). ORCA025-N102 includes the ocean circulation model OPA9 (Madec et al. 1998) coupled to the Louvain-la-Neuve Ice Model sea ice model LIM2 (Fichefet and Morales Maqueda 1997). The ocean model is configured on a tri-polar Arakawa C-grid (Arakawa 1966) with the model poles at the geographical South Pole, in Siberia and in the Canadian Arctic Archipelago (CAA). The horizontal resolution is approximately 28 km at the equator, increasing to 6–12 km in zonal and ~3 km in meridional directions in the Arctic Ocean. The model resolves large eddies (~30–50 km), while "permitting" most of smaller eddies. ORCA025-N102 has a higher vertical resolution than the ORCA025-G70 configuration, utilizing 64 vertical levels with thicknesses ranging from approximately 6 m near the surface to 204 m at 6,000 m. The high vertical resolution in the upper ocean (8 levels in the upper 50 m and 13 levels in the upper 100 m) greatly improves the model representation of the shallow Arctic continental shelves, Bering and Chukchi Seas. There are eight model cells across Bering Strait (Fig. 7.1e). The fine model resolution in the both, horizontal and vertical, together with high resolution model bathymetry adapted from ETOPO2 and partial steps in the model bottom topography accurately approximates the steep seabed relief near the Arctic shelves, resulting in the more realistic along-shelf flow (e.g., Barnier et al. 2006; Penduff et al. 2007). The LIM2 sea ice model uses the Viscous-Plastic (VP) ice rheology (Hibler 1979) and the 3-layer Semtner (1976) thermodynamics updated with sub-grid scale sea ice thickness distribution (Fichefet and Morales Maqueda 1997) and sea ice thickness-dependent albedo (Payne 1972). To obtain more distinct sea ice edges, the model employs the positive-definite, second moments conserving advection scheme by Prather (1986). The sea ice model is coupled to the ocean model every five oceanic time steps through a non-linear quadratic drag law (Timmermann et al. 2005).

For the 1958–2001 simulations used in the present study, the ORCA025 model was driven by the DRAKKAR Forcing Set (DFS 3.1) atmospheric reanalysis (Brodeau et al. 2010). The reanalysis combines monthly precipitation, daily downward shortwave and longwave radiation from the CORE forcing data set (Large and Yeager 2004) and 6-hourly 10 m wind, 2 m air humidity and 2 m air temperature from ERA40 reanalysis. The turbulent exchanges between atmosphere and ocean and atmosphere and sea ice are computed during model integration using the bulk formulae from Large and Yeager (2004). Climatological monthly continental runoff (Dai and Trenberth 2002) is included as an additional freshwater source, applied along the coastline. Initial conditions for temperature and salinity are derived from a monthly climatology that merges the Levitus et al. (1998) World Ocean Atlas climatology with the PHC2.1 database (Steele et al. 2001) in high latitudes. To avoid salinity drift, the sea surface salinity is restored toward the monthly mean climatological values on the timescale of 180 days for the open ocean and 12 days under sea-ice.

7.2.5 *Pan-Arctic Ice-Ocean Modeling and Assimilation System (PIOMAS)*

PIOMAS is a variant of BESTMAS (see description above) with a coarser horizontal resolution (~40 km) and smaller model domain (north of 49°N; Zhang et al. 2008). However, it has 12 categories each for ice thickness, enthalpy, and snow depth (Zhang et al. 2008). The centers of the 12 ice thickness categories are 0, 0.26, 0.71, 1.46, 2.61, 4.23, 6.39, 9.10, 12.39, 16.24, 20.62, and 25.49 m. The model bathymetry in the vicinity of Bering Strait and the location of the Bering Strait cross-section are shown in Fig. 7.1f.

7.3 Bering Strait Observational Mooring Data

Year-round moorings have been deployed in the strait almost continuously since 1990 (see Woodgate et al. 2006, 2010; and http://psc.apl.washington.edu/BeringStrait.html), generally at 2–4 locations, as shown in Fig. 7.1a. Site A1 is in the western channel of the strait and thus in the Russian EEZ. Access was only granted to this site in the early 1990s (data available from 1990 to 1991; 1992 to 1993, 1993 to 1994) and since 2004. Site A2 is in the eastern portion of the strait (U.S. waters). A third site, A3, was established in 1990 at a site just north of the strait (and in the US EEZ), hypothesized to provide a useful average of the flow through both of the channels (Woodgate et al. 2005a, b, 2006, 2007). For some years (1992–1993, 1993–1994, 1994–1995) the A3 mooring was deployed ~120 nm further north, but these data are not considered here. Observations from A2 and A3 are available since autumn 1990, except for a few missing months, and for the deployment year autumn 1996–1997 when no moorings were deployed in the strait. A fourth mooring site A4, was established near the U.S. coast in 2001 to measure the Alaskan Coastal Current (Woodgate and Aagaard 2005; see discussion below). A high-resolution array was deployed in the strait starting in 2007; for more details see http://psc.apl.washington.edu/BeringStrait.html.

Since the region is ice-covered in winter, all mooring instrumentation has traditionally been kept near-bottom to avoid damage by ice keels. The moorings provide measurements of temperature, salinity and velocity approximately 10 m above bottom. High correlation (0.95; Woodgate et al. 2005b) in velocity is found between all sites in the strait region (Woodgate et al. 2005b) suggesting that extrapolation of velocity between mooring sites is reasonable. All available ADCP data (some moorings, and ship-based ADCP sections from the eastern channel) and newer mooring data, show strong coherence in the vertical (see e.g., Roach et al. 1995, where the first EOF at a central channel site explains 90 % of the variance), with some surface intensification of the flows, especially within the Alaskan Coastal Current. Thus, assuming the near-bottom flow correlates well with the total volume transport also seems reasonable (see Woodgate et al. 2005b for a discussion).

In terms of water properties, the near-bottom data do not capture the upper layer, which in the summer/autumn period of the year is likely 10–20 m thick, about 1–2 °C warmer and about 1 psu fresher than the lower layer (Woodgate and Aagaard 2005; Woodgate et al. 2010).

The flow through the Bering Strait is generally believed to be driven by some far field forcing (often described as the pressure head forcing) modulated by local wind effects (see Woodgate et al. 2005b for discussion and historic references). Woodgate et al. (2005b) suggest this large-scale forcing likely explains the high velocity correlation between sites. On the Alaskan Coast on the edge of the eastern channel there is seasonally a strong surface-intensified current. This is the Alaskan Coastal Current, which is present from midsummer until about the end of the year (Paquette and Bourke 1974; Ahlnäs and Garrison 1984; Woodgate and Aagaard 2005), and in summer CTD sections it is present as a ~10 km wide, 40 m deep warm, fresh current (Woodgate and Aagaard 2005). Much less is known about the Siberian Coastal Current (SCC), which is present sometimes on the Russian coast (Weingartner et al. 1999). Observations from the western side of Bering Strait indicate that the SCC can, at times, flow southward here under strong northerly winds. These events tend to occur during autumn and winter and appear to be short-lived (1–10 days; Weingartner et al. 1999). The SCC transport is estimated to be small (~0.1 Sv; Weingartner et al. 1999).

7.4 Results

Model representations of the geographical width across Bering Strait range from 90 to 160 km (Fig. 7.2), in part due to the choice made of the representative section in the model. ORCA and PIOMAS have widths most similar to reality (~85 km), while BESTMAS, NAME, and ECCO2 are wider than reality. The various horizontal resolutions from the five models and the different bathymetry schemes make the results appear disparate upon first glance. In fact the cross-sectional area of the strait varies from 2.4 to 4.5 km^2 for the models (Table 7.2). However, a closer look suggests agreement that horizontal shear is frequently present in the model results and that the highest speeds tend to be in the eastern channel. It is likely that this is at least in part an artifact due to the way the model sections cross the bathymetry, with the ends of the sections being either north or south of the strait proper. Certainly, observational results (e.g., Woodgate et al. 2005b) show no significant differences in the near-bottom velocity between the two channels away from the ACC. Vertical shear is present in some model results, particularly the NAME, ECCO2, and ORCA models. In NAME, the velocity tends to increase from surface to bottom, in contrast to other models. It appears that the velocity maxima are located deeper in the channels where frictional effects are less, as compared to the surface and nearby the coasts.

We also present northward velocity, temperature, and salinity sections for the summer period (Jul.–Sep.) from the five models (Figs. 7.3, 7.4, and 7.5). Strong vertical mixing is expected during the winter period within the northern Bering Sea

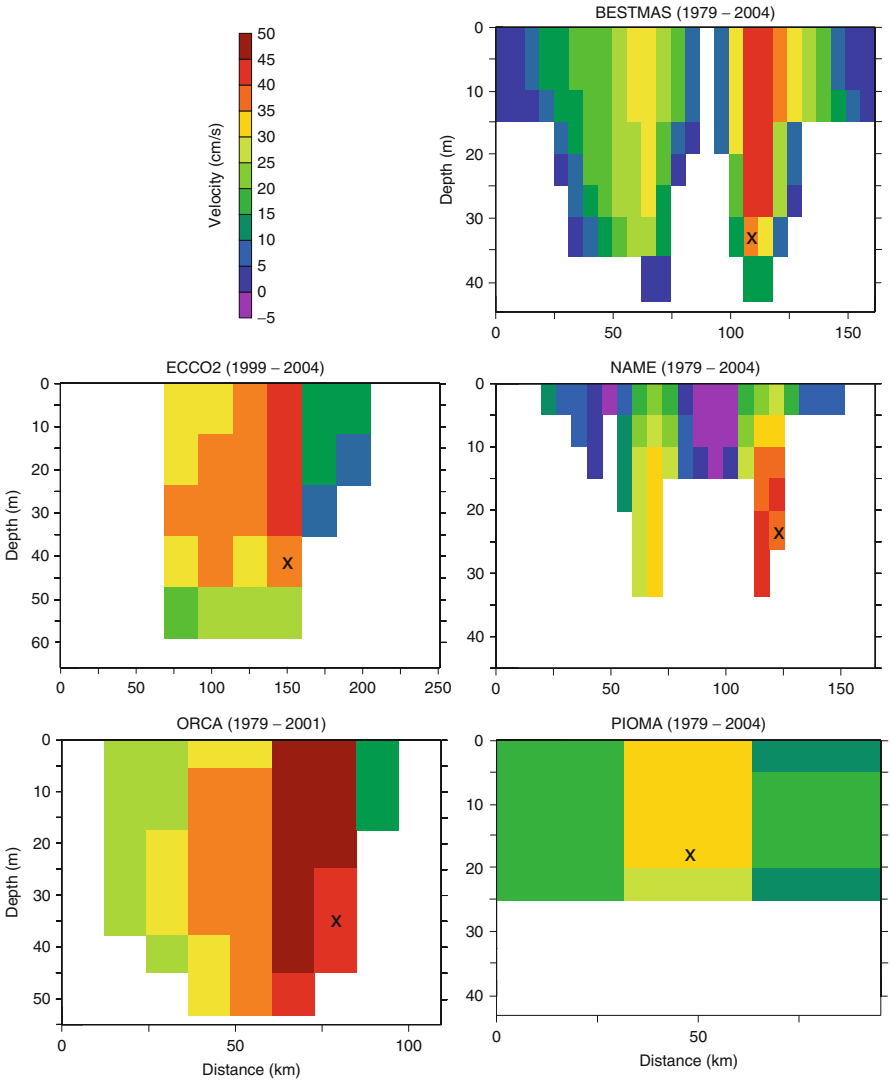

Fig. 7.2 Vertical section of the long-term mean northward velocity (cm/s) across Bering Strait from all models. Positive velocity is northward. A *black X marks* the approximate location of the A2 mooring within each model domain

(Clement et al. 2004; Woodgate and Aagaard 2005). Therefore, we present the mean summer results for comparison. The mean summer velocity sections from the models show slightly higher speeds than the long-term annual mean, especially in the upper water column (Fig. 7.3). There tends to be less vertical shear in the mean summer sections, as compared to the long-term mean sections (Fig. 7.2). Temperature sections (Fig. 7.4) indicate higher values in the upper water column near the Alaskan

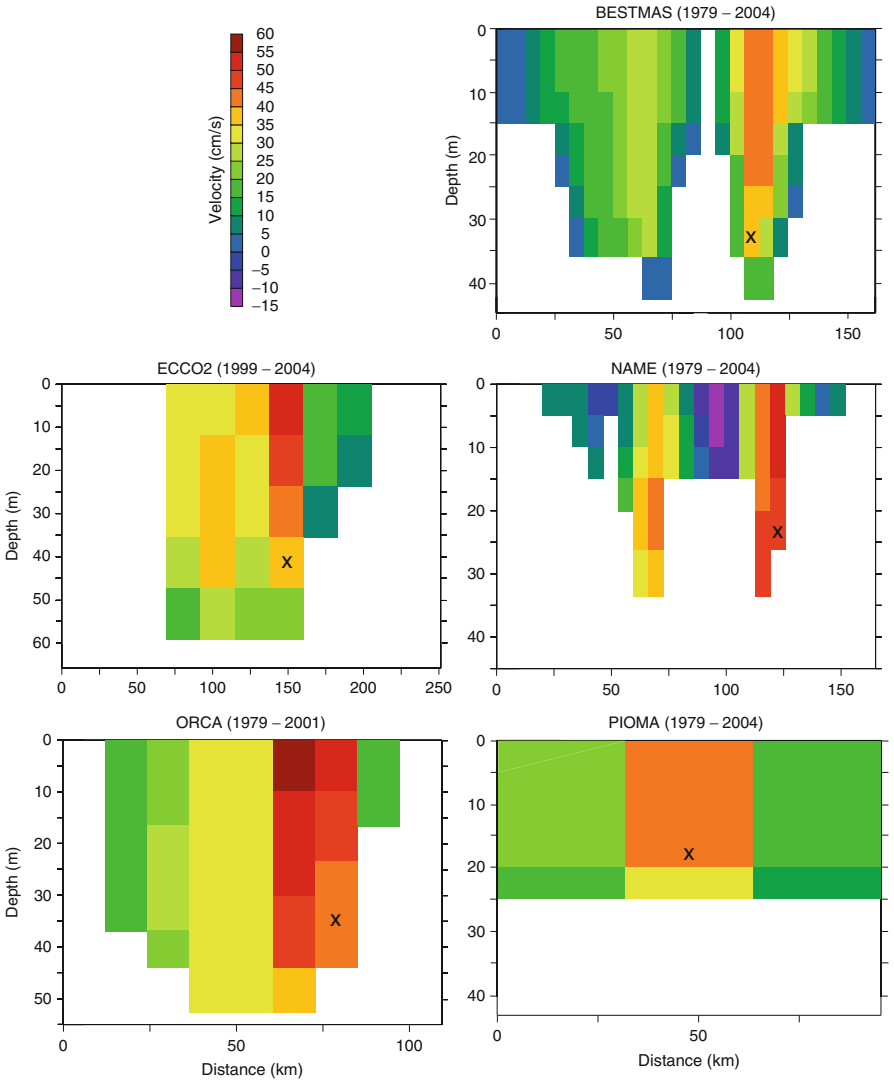

Fig. 7.3 Vertical section of the long-term summer (Jul.–Sep.) mean northward velocity (cm/s) across Bering Strait from all models. Positive velocity is northward. A *black X marks* the approximate location of the A2 mooring within each model domain

coast. BESTMAS and NAME have temperature values up to ~10 °C here. Similarly, for salinity (Fig. 7.5) an east–west gradient is present with the lower values found on the eastern side. Particularly, ECCO2, BESTMAS, and NAME show salinities less than 30 psu in this location. Multiple summertime CTD sections of temperature and salinity (http://psc.apl.washington.edu/BeringStrait.html) indicate elevated temperature and decreased salinity nearby the U.S. coast due to the presence of the

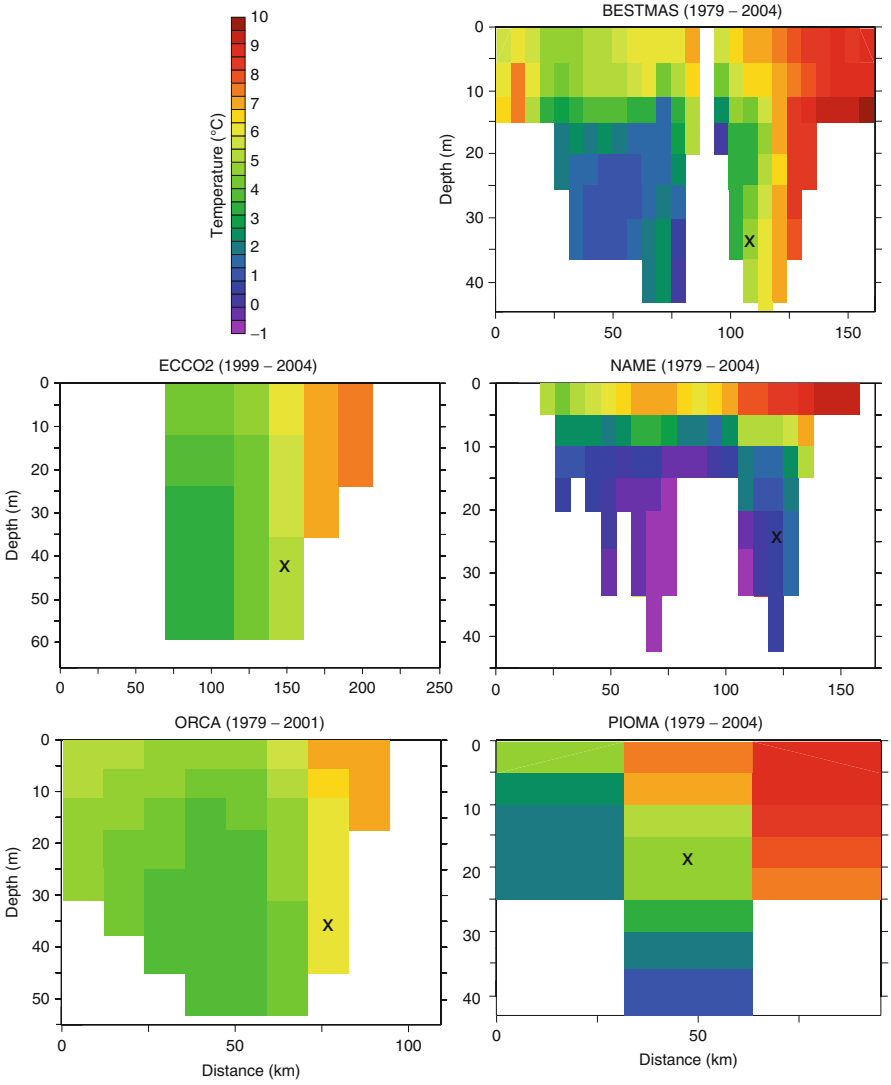

Fig. 7.4 Vertical section of the long-term summer (Jul.–Sep.) mean temperature (°C) across Bering Strait from all models. A *black X marks* the approximate location of the A2 mooring within each model domain

Alaska Coastal Current (ACC). The width of this current is on the order of ~10 km and, therefore, it is not properly resolved by the models due to spatial resolution limitations. However, model results do show the proper east–west gradients in temperature and salinity, as expected from observations (see e.g., Coachman et al. 1975).

To compare with long-term moored observations, we present monthly mean northward near-bottom velocity at sites A2 and A3 for models (color) and data

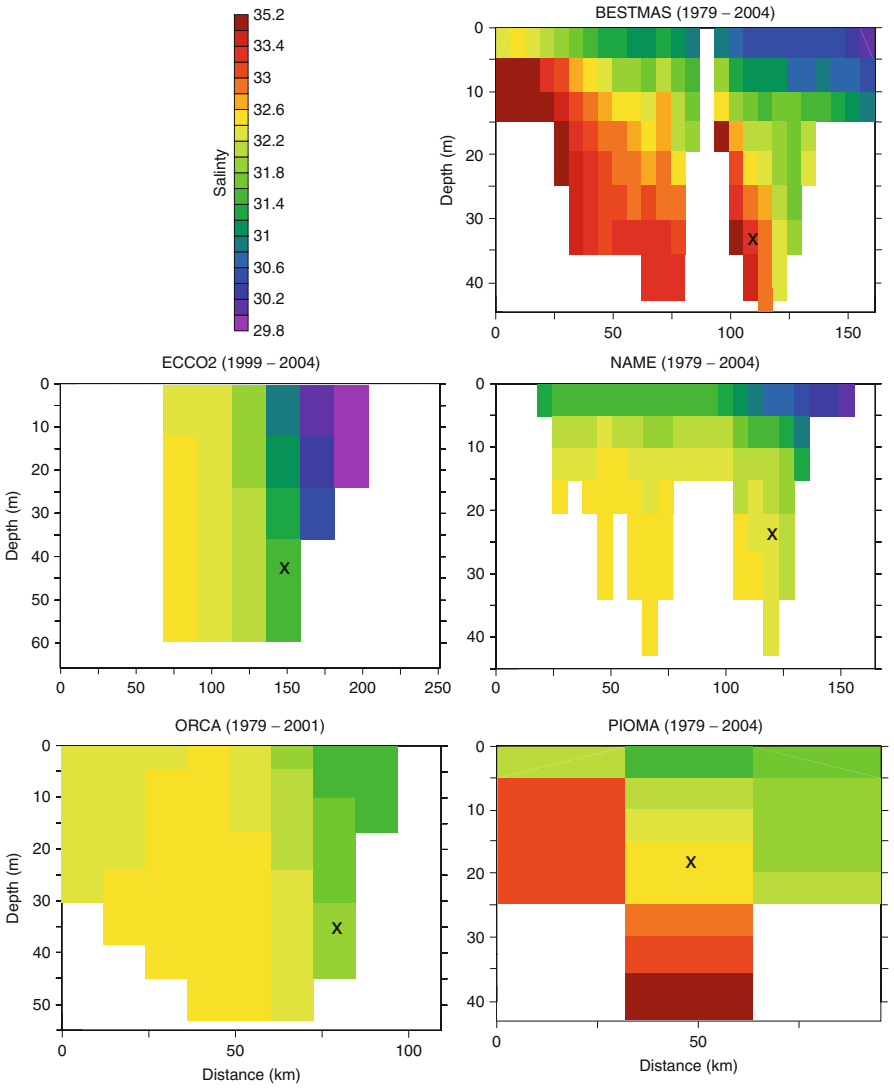

Fig. 7.5 Vertical section of the long-term summer (Jul.–Sep.) mean salinity (psu) across Bering Strait from all models. A *black X marks* the approximate location of the A2 mooring within each model domain

(black) for 1979–2004 in Fig. 7.6. For A2 (eastern channel, Fig. 7.1a), model velocities range from ~5 cm/s southward to over 80 cm/s northward. Predominantly, the flow is northward with the mean northward velocity ranging from 28.6 (+/−1.0) to 40.1 (+/−1.9) cm/s among models, over the time period when observations are available (Table 7.3). The range is 29.5 (+/−0.49) to 43.2 (+/−0.88) cm/s over the larger 1979–2004 time period (Table 7.4.) Two of the lower resolution models (ORCA and ECCO2) have the highest velocities, while the higher resolution

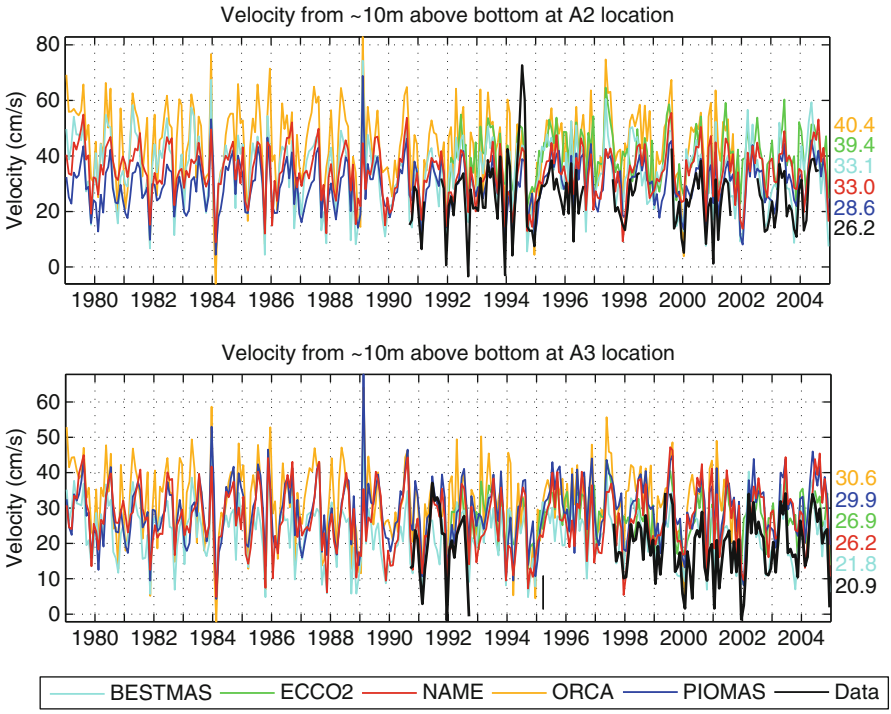

Fig. 7.6 Monthly mean velocity at ~10 above the bottom from the A2 mooring location (*upper*) and A3 mooring location (*lower*). Model results are shown in *color* and the observations are shown in *black*. Mean values for the time period when data are available are shown on the far right

models (BESTMAS and NAME) have lower velocities. The observed mean northward velocity is 26.2 (+/−2.8) cm/s, which matches the lower range of the modeled mean values. All of the models show a significant (at the 99 % level) correlation with the observed velocities at this location. The correlation coefficients range from 0.67 to 0.78 for the monthly means at A2 (Table 7.5).

Figure 7.3b shows the near-bottom northward velocity at the A3 location. The model spread of velocities is slightly narrower for A3, with the BESTMAS model having the lowest mean velocity (21.8 +/− 0.8 cm/s) and ORCA having the highest mean velocity (30.6 +/− 1.3 cm/s) over the same time period as observations. The observed mean northward velocity is 20.9 +/− 2.3 cm/s. The correlations between the models and the data at A3 are significant (at the 99 % level), with correlation coefficients ranging between 0.70 and 0.82 (Table 7.5).

It is important to recognize that a comparison between point measurements and model results is difficult. In the data, velocity is measured at a single point, while in models it is a grid-cell mean, which may range from a few to tens of kilometers in the horizontal and several meters in the vertical. In addition, the discrepancy

Table 7.3 Mean velocity, volume transport, near-bottom temperature, and near-bottom salinity from the models and from observations, for the time period when observations are available, as shown in Figs. 7.3 and 7.4

Model/data	Mean velocity ~10 m above bottom at the A2 location (cm/s)	Mean velocity ~10 m above bottom at the A3 location (cm/s)	Mean volume transport (Sv)	Mean temperature ~10 m above bottom at the A2 location (°C)	Mean temperature ~10 m above bottom at the A3 location (°C)	Mean salinity ~10 m above bottom at the A2 location (psu)	Mean salinity ~10 m above bottom at the A3 location (psu)
BESTMAS	**33.1** (1.3)	**21.8** (0.8)	**0.69** (0.03)	**0.79** (0.25)	**0.65** (0.24)	**33.16** (0.06)	**33.20** (0.06)
Data	**26.2** (2.8)	**20.9** (2.3)	**0.80** (0.20)[a]	**0.27** (0.3)	**–0.11** (0.2)	**32.26** (0.08)	**32.49** (0.06)
ECCO2	**39.4** (1.2)	**26.9** (0.7)	**1.06** (0.03)	**1.10** (0.27)	**0.62** (0.23)	**31.72** (0.06)	**32.29** (0.04)
NAME	**33.0** (1.0)	**26.2** (0.7)	**0.67** (0.03)	**–0.96** (0.09)	**–1.26** (0.05)	**32.45** (0.04)	**32.61** (0.04)
ORCA	**40.4** (1.9)	**30.6** (1.3)	**1.29** (0.06)	**0.96** (0.25)	**0.79** (0.24)	**32.30** (0.05)	**32.47** (0.03)
PIOMAS	**28.6** (1.0)	**29.9** (0.9)	**0.81** (0.03)	**0.34** (0.21)	**0.60** (0.23)	**33.09** (0.05)	**32.80** (0.05)

However, the values from ECCO2 are for 1992–2004 only and the values from ORCA are for 1990–2001 only. Error estimates are shown in parenthesis. All model errors are calculated as the standard error of the mean (sample standard deviation divided by the square root of the sample size)

[a]The uncertainty for the data estimate is ~25 % (Woodgate et al. 2005a, b)

Table 7.4 Long-term mean velocity, volume transport, near-bottom temperature, and near-bottom salinity from the models, for the time periods shown in Figs. 7.3 and 7.4

Model/data	Mean velocity ~10 m above bottom at the A2 location (cm/s)	Mean velocity ~10 m above bottom at the A3 location (cm/s)	Mean volume transport (Sv)	Mean temperature ~10 m above bottom at the A2 location (°C)	Mean temperature ~10 m above bottom at the A3 location (°C)	Mean salinity ~10 m above bottom at the A2 location (psu)	Mean salinity ~10 m above bottom at the A3 location (psu)
BESTMAS	**34.0** (0.69)	**22.8** (0.45)	**0.72** (0.02)	**0.76** (0.17)	**0.71** (0.16)	**33.18** (0.05)	**33.17** (0.04)
ECCO2	**39.9** (0.78)	**27.4** (0.52)	**1.07** (0.02)	**1.08** (0.25)	**0.63** (0.20)	**31.72** (0.05)	**32.25** (0.03)
NAME	**34.1** (0.52)	**27.0** (0.65)	**0.65** (0.01)	**−1.02** (0.06)	**−1.27** (0.03)	**32.46** (0.02)	**32.58** (0.02)
ORCA	**43.2** (0.88)	**31.6** (0.65)	**1.33** (0.03)	**0.89** (0.17)	**0.69** (0.15)	**32.33** (0.02)	**32.47** (0.02)
PIOMAS	**29.5** (0.49)	**29.2** (0.49)	**0.79** (0.02)	**0.26** (0.14)	**0.53** (0.15)	**33.13** (0.03)	**32.78** (0.03)

Error estimates are shown in parenthesis

Table 7.5 Correlation coefficients between models and the observations of velocity, temperature, and salinity at A2 and A3 locations

	Velocity		Temperature		Salinity	
Model	A2	A3	A2	A3	A2	A3
BESTMAS	0.78	0.71	0.78	0.70	0.67	0.53
ECCO2	0.67	0.72	0.77	0.76	0.60	0.48
NAME	0.69	0.75	0.73	0.86	0.70	0.57
ORCA	0.68	0.70	0.79	0.76	0.60	0.39
PIOMAS	0.70	0.82	0.88	0.79	0.66	0.59

All correlations are significant at the 95 % level

Table 7.6 Depth information (m) for the models and the observations at the A2 and A3 mooring locations

Location	Model/data	Water column depth (m)	Mid-depth of model grid cell or depth of observation ~10 m above bottom (m)
A2	Data	53	44
	BESTMAS	51	39.5
	ECCO2	50	35
	NAME	53	37.7
	ORCA	57.9	35.5
	PIOMAS	43	33
A3	Data	56	47
	BESTMAS	51	39.5
	ECCO2	50	35
	NAME	53	37.7
	ORCA	57.9	35.5
	PIOMAS	43	33

between the real and model bathymetry introduces a difference in bathymetric gradients, displacing model currents from their "true" geographical positions. Choice of model section location is also very important, for example, there will be obvious discrepancies between an observational section taken across the narrowest point of the strait and a model section crossing shallow regions to the north or south of the strait. Table 7.6 and Fig. 7.2 illustrate these points. Table 7.6 shows the depth at the moorings A2 and A3 and model depth at the co-located virtual moorings; the difference between real and model bathymetry is clear. Moreover, in the models, velocity can vary significantly between the adjacent model grid cells (Fig. 7.2), although this is not seen in observations outside the ACC. Thus the results of a model-observations comparison would depend upon the exact geographical position of model virtual moorings. Finally, the stochastic nature of the oceanic turbulence cannot be simulated by the models used in this study. Therefore, it is likely more informative to evaluate model results using integrated fluxes, as discussed below.

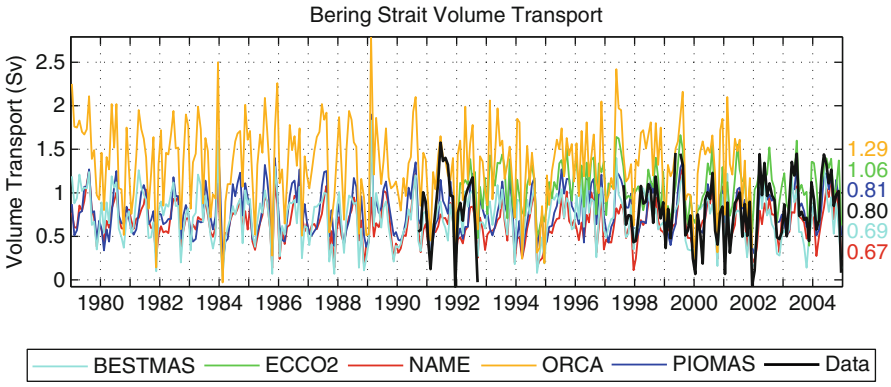

Fig. 7.7 Monthly mean volume transport from the models and observations. The observations are based on the near-bottom velocity at the A3 mooring location multiplied by a cross-sectional area of 4.25 km^2, as per Woodgate et al. (2010). Mean values for the time period when data are available are shown on the far right

Monthly mean Bering Strait volume transport from the models and observations is shown in Fig. 7.7. The observations are based on the near-bottom velocity at the A3 mooring location multiplied by a cross-sectional area of 4.25 km^2, as per Woodgate et al. (2010). Model means range from 0.67 (+/−0.03) to 1.29 (+/−0.06) Sv (Table 7.3) over the time period when observations are available. The volume transport is highest for the ORCA and ECCO2 models and is lowest for the PIOMAS, BESTMAS and NAME models. The observed estimate of the long-term mean (1991–2004) volume transport through Bering Strait is 0.8 +/− 0.2 Sv (Woodgate et al. 2005a). This estimate is based on observations at the A3 mooring location, although numbers do not differ significantly if using observations from the other mooring sites.

Near-bottom monthly mean temperatures at the A2 and A3 mooring locations are shown in Fig. 7.8. (Temperature at A1 is not shown because there are too few data available at this time.) Temperatures tend to be warmer at the southern A2 location, with model means ranging between −0.96 (+/−0.09) and 1.1 (+/−0.27) °C. The mean observed near-bottom temperature for the same location is 0.27 (+/−0.3). ORCA, ECCO2, and BESTMAS models tend to overestimate the temperature by 0.5–0.8 °C in the mean, while NAME underestimates the temperature by 1.2 °C in the mean. We speculate that the colder temperatures for the NAME model may be related to excessive ice production, especially in polynya regions of the northern Bering Sea. Surprisingly, the PIOMAS temperatures are closest to the observed, despite the fact that it is the lowest resolution model in this study and only has 3 grid points across the strait (Fig. 7.2). Temperatures at the A3 location are, again, underestimated in the NAME model and overestimated in ORCA, ECCO2, BESTMAS and also in PIOMAS. While the magnitude of the model-data differences may be up to ~1 °C in the mean, the models' results are significantly correlated (at the 99 % confidence level) with

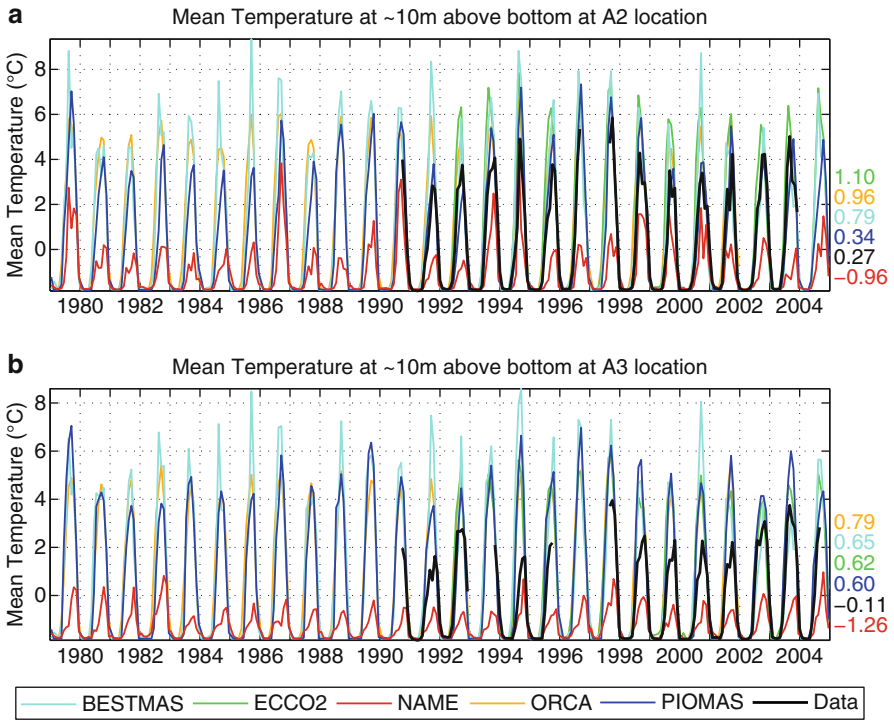

Fig. 7.8 Monthly mean near-bottom temperature (°C) at the (**a**) A2 and (**b**) A3 mooring locations. Model results are shown in *various colors* and observations are shown in *black*. Mean values for the time period when data are available are shown on the far right

the observations. The correlation coefficients range between 0.73 and 0.88 at A2 and between 0.70 and 0.86 at A3 (Table 7.5). There is no trend, either observed or modeled, in the time series shown here. There is, however, a strong seasonal cycle present, which enhances the correlations. The seasonal cycle has been identified by many authors (e.g. Fedorova and Yankinam 1964; Coachman et al. 1975; Roach et al. 1995 and references therein) and was later quantified into a modern climatology by Woodgate et al. (2005a). This seasonal cycle will be discussed below.

A similar analysis was performed for salinity at the A2 and A3 mooring locations (Fig. 7.9). The mean modeled salinity ranges between 31.7 (+/−0.06) and 33.2 (+/−0.06) psu at A2 and between 32.2 (+/−0.04) and 33.2 (+/−0.06) psu at A3. The mean observed salinities are 32.3 (+/−0.08) at A2 and 32.5 (+/−0.06) at A3. The BESTMAS and PIOMAS models tend to overestimate the salinity, by up to 0.9 psu above the observed mean value, whereas the NAME, ECCO2, and ORCA models have values close to the observed. All of the models' results are significantly correlated (at the 99 % confidence level) with the observations of salinity at A2 and

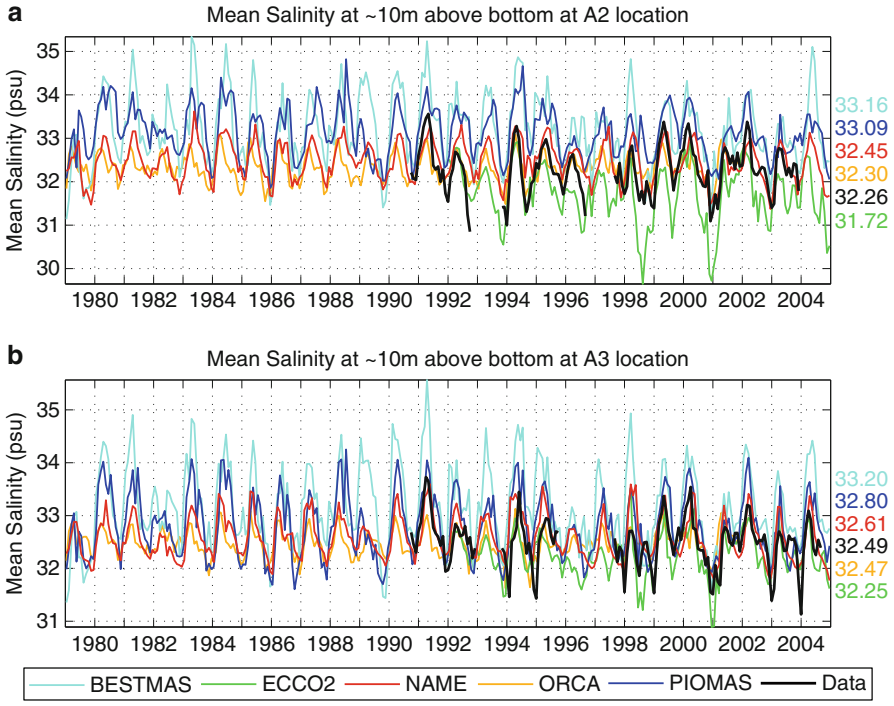

Fig. 7.9 Monthly mean near-bottom salinity at the (**a**) A2 and (**b**) A3 mooring locations. Model results are shown in *various colors* and observations are shown in *black*. Mean values for the time period when data are available are shown on the far right

A3. The correlation coefficients range between 0.60 and 0.70 at A2 and between 0.39 and 0.59 at A3 (Table 7.5). The correlations are not as high for salinity as they are for temperature, especially at the A3 location. Again, a seasonal cycle of salinity is apparent in the time series (also see Woodgate et al. 2005a), however it is not as strong as the seasonal cycle of temperature.

Annual mean volume transport from models and observations is shown in Fig. 7.10a. Observed volume transport (not including the ACC) ranges from 0.6 to 1 Sv (+/−0.2 Sv, Woodgate et al. 2006), which is most similar to the estimates from the BESTMAS, NAME, and PIOMAS models. The ACC likely adds around 0.1 Sv to the estimates (Woodgate and Aagaard 2005), thus the true flux is likely slightly higher than shown in Fig. 7.10a, and closer to the ECCO2 values.

Heat fluxes through Bering Strait and through the Chukchi shelf appear to influence the distribution and thickness of sea ice (Coachman et al. 1975; Shimada et al. 2006; Woodgate et al. 2010). Previously published observations of heat flux (e.g., Woodgate et al. 2010) use a reference temperature of −1.9 °C. Therefore, for the model calculations, we used the same value for a reference temperature. However, we note that the PIOMAS and BESTMAS models use −1.8 °C as the freezing temperature for an ease in conserving heat in the models. Oceanic heat flux through

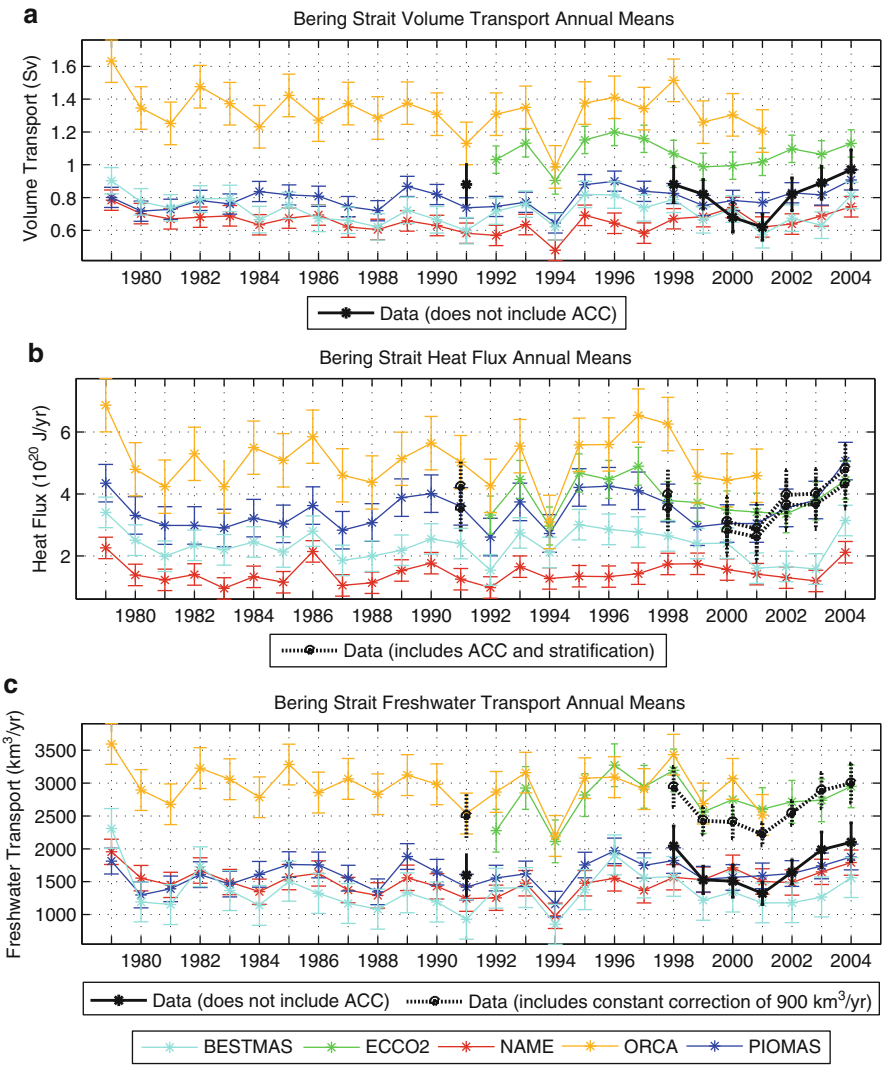

Fig. 7.10 Annual mean (**a**) volume transport, (**b**) heat, and (**c**) freshwater fluxes. Heat flux is referenced to −1.9 °C for the models, in order to compare with cited observations in the text. Freshwater is referenced to 34.8 psu. Observed volume transport values (**a**) do not include the ACC and stratification, which likely add ~0.1 Sv (see Woodgate et al. 2006). The observed heat flux values (**b**) include an estimate for the ACC using SST for a 10 m surface layer (*lower bound*) and a 20 m surface layer (*upper bound*). Observed heat flux values are described further in Woodgate et al. (2010). The *dashed black line* (**c**) represents the observed freshwater flux with an estimated ACC and stratification correction of an additional 900 km³/year (Woodgate et al. 2006)

Bering Strait in the models was calculated as the vertical and horizontal integral of: the heat (heat capacity multiplied by the difference between the temperature and the reference temperature) multiplied by velocity normal to the cross-section on a monthly mean time scale.

The annual mean oceanic heat flux time series for the models and observations (as per Woodgate et al. 2010) are shown in Fig. 7.10b. In the models, peaks in the heat flux occurred during several years (e.g., 1979, 1986, 1993, and 1997) and consistently showed up in results from all five models. However, data coverage is not sufficient to confirm these peaks in the real world. A peak in 2004 is noted in observations (see Woodgate et al. 2010) and is apparent in all of the models, except ORCA, which does not have results for that time period. ECCO2 is also able to simulate a recent increase in heat flux in 2007 (not shown), similar to the observations (Woodgate et al. 2010).

The long-term model mean heat flux ranged between 1.5×10^{20} J/year and 5.1×10^{20} J/year. This is, admittedly, a wide range of values. ORCA and ECCO2 have much higher values than BESTMAS and NAME. Observations of the annual heat flux based on near-bottom measurements, a correction for the ACC, and SST from satellite data were published in Woodgate et al. (2010). The observed range of heat flux estimates is ~2.8–4.5×10^{20} J/year with estimated uncertainty of 0.8×10^{20} J/year, based on years 1991, 1998, 2000–2006. However, the 2007 heat flux was estimated at 5–6×10^{20} J/year.

Freshwater flux from the Bering Sea into the Chukchi Sea is an important factor affecting stratification and the maintenance of the Arctic Ocean halocline (e.g., Aagaard et al. 1985a). As discussed in Aagaard et al. (2006), the salinity field in Bering Strait is influenced by a number of processes primarily within the Bering Sea, including inflow from the Gulf of Alaska, on-shelf transport from the deep basin, precipitation minus evaporation, river runoff, and formation/degradation of sea ice. The combined net effect of these processes determine, in large part, the downstream salinity (and to a lesser extent freshwater fluxes) found in the strait. For the calculation of freshwater fluxes, a reference salinity of 34.8 psu was used because this value is considered to be the mean salinity of the Arctic Ocean and has been used in most other Arctic studies (based on original work by Aagaard and Carmack 1989). Integrated annual mean oceanic freshwater fluxes were calculated on a monthly mean timescale (see Eq. 1 in Melling 2000) from each of the models and are shown in Fig. 7.10c. An observationally-based lower bound of annual mean freshwater fluxes is also shown, however these values do not include the ACC or stratification and thus likely underestimate the freshwater flux by about 800–1,000 km^3/year (Woodgate et al. 2006). With this correction, the observed freshwater annual means are similar to results from the ECCO2 and ORCA models, with the other models appearing to underestimate the total freshwater flux. No long-term trend is apparent in either the heat or freshwater flux for this time period, however a gradual increase in freshwater during the early 2000s has occurred in the model results, ending with a peak in freshwater flux in 2004, similar to observations (also see Woodgate et al. 2006, 2010).

It is important to note that both the models and the data have limitations with respect to calculations of heat and freshwater fluxes. The models used here are too coarse to represent the narrow (~10 km) ACC, which is estimated to carry 25 % of the freshwater flux and 20 % of the heat flux (Woodgate et al. 2006) through the

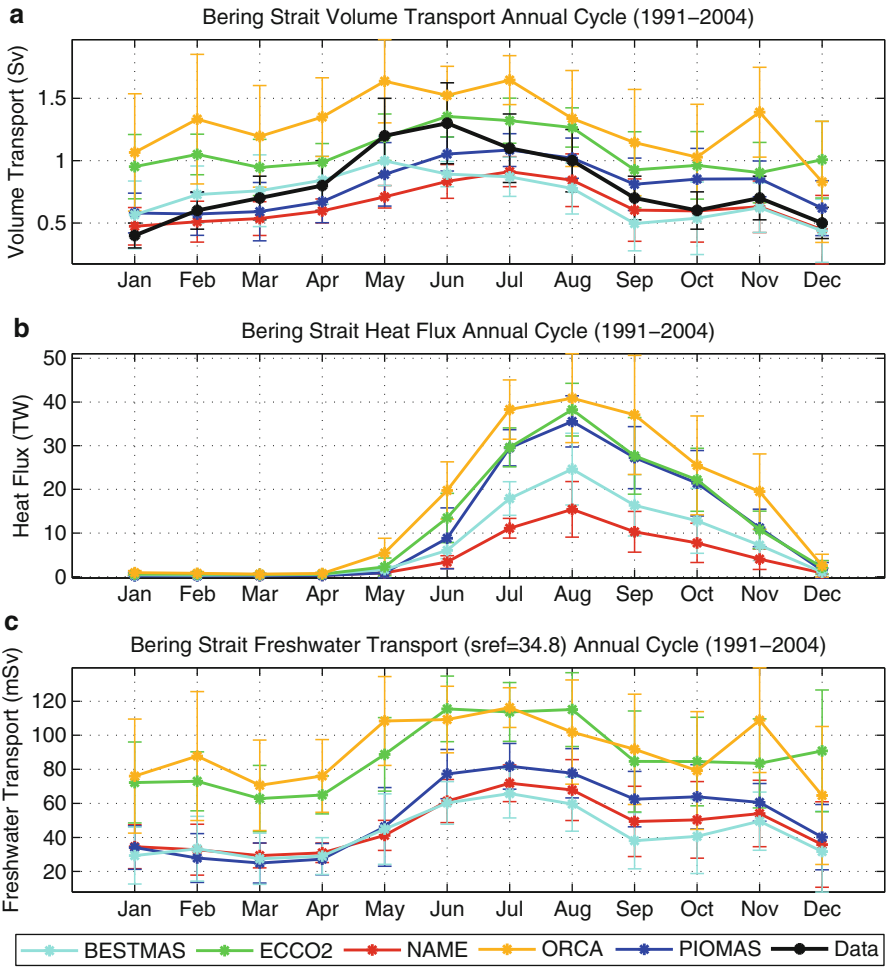

Fig. 7.11 Seasonal cycles of (**a**) volume transport, (**b**) heat flux, and (**c**) freshwater transport. The seasonal cycles are averaged over 1991–2004, except for ORCA (1991–2001) and ECCO2 (1992–2004). Heat flux is referenced to −1.9 °C for the models, in order to compare with cited observations in the text. The freshwater transport is referenced to 34.8 psu

strait. The historic near-bottom data used here does not measure the ACC, which is a surface/coastal feature. Thus, on-going research is using extra moorings, hydrographic data and upper water column sensors to estimate stratification (see e.g., http://psc.apl.washington.edu/BeringStrait.html).

Arctic shelf seas have a strong seasonal cycle of temperature and salinity; some areas may also exhibit strong seasonal changes in the oceanic circulation. The Bering Strait region is no different in this respect. Observations have shown

stronger northward flows in summer (e.g., Coachman and Aagaard 1988; Roach et al. 1995; Woodgate et al. 2005a, b). According to the model results, volume transport peaks in summer (May–July) and is lowest in winter (December–March; Fig. 7.11). This agrees reasonably with observational results (peaking in May/Jun, minimum in Dec–Feb; although variability is high; Woodgate et al. 2005a). In general, the data have a larger seasonal cycle, with a range of 0.4–1.3 Sv (errors order 25 %; Woodgate et al. 2005a, b). PIOMAS, BESTMAS, ECCO2, and NAME models have similar seasonal cycles to the data, however they are not as strong.

As shown by Woodgate et al. (2010), the heat flux seasonal cycle is also very strong. Observational results (see Fig. 3 of Woodgate et al. 2010) suggest strong interannual variability in the timing of the summer peak, although the computation presented there does not include the seasonality of the ACC. In the models (Fig. 7.11), heat flux peaks in summer and is near-zero in winter. However, the models do not agree on the magnitude of the summertime peak, which ranges between 15 (+/−6.4) to over 40 (+/−14) TW. The heat flux is near zero for December–April (when water temperatures are around freezing). The models with the highest resolutions (BESTMAS and NAME) show lower peaks in the summertime heat flux [15 (+/−6.4) and 22.5 (+/−7.9) TW], while the lower resolution models have higher heat fluxes.

Seasonal cycles of freshwater flux through Bering Strait are similar for PIOMAS, BESTMAS, and NAME, with peaks in the summer (June–August) and lowest in winter (December–April). Again, interannual variability makes these peaks less certain. The freshwater flux maxima for these models are between 65 (+/−14.3) and 80 (+/−13.4) mSv in July. Seasonal cycles for ECCO2 and ORCA have somewhat similar shapes, however they transport more freshwater (up to 115 (+/−11.7) mSv in summer and more than 60 (+/−40) mSv in winter for ORCA) to the north.

7.5 Discussion

Model volume transports ranged from 0.67 (+/−0.03) to 1.29 (+/−0.06) Sv in the mean, compared to observational estimates of 0.8 +/−0.2 Sv; the observations may still underestimate the ACC contribution. Thus, most of the models are in agreement with the observational estimate to within errors. ORCA and ECCO2 showed the highest volume transports, while NAME and BESTMAS showed the lowest transports. Oddly, higher resolution models seem to give lower transport estimates; we do not fully understand why this is. Note that of the models, ORCA and ECCO2 also have the largest cross sectional area of the strait. The cross-sections in each model were chosen to approximate the locations of moored observations as closely as possible (Fig. 7.1), however different cross-sectional areas would arise from choosing a slightly different position of the section. The models are using both lateral and vertical friction parameterization to represent the flow next to the boundary (bottom/surface or lateral; see Table 7.2). Some uncertainty of model estimates of the volume transport throughout the strait might be related to the estimation of the frictional layers, subject to the parameterization used. Penduff et al. (2007) have

demonstrated that enstrophy-conserving momentum advection schemes produce a spurious numerical sidewall friction, leading to a weaker topographic alignment of the mean flow and weaker barotropic transports. They reported a ~10 % reduction in Bering Strait transports in simulations with the enstrophy conserving advection, compared to the runs with the energy-enstrophy conserving scheme, characterized by low numerical friction. The effect of spurious friction on transports is similar to the one of explicit lateral friction. Both spurious sidewall and explicit non-slip lateral friction could explain lower transports in BESTMAS and NAME models compared to ECCO2 and ORCA, as the last two models feature free-slip lateral boundary conditions. Besides, ORCA utilizes energy-enstrophy conserving advection, which may result in higher transport than in ECCO2 (Tables 7.3 and 7.4). However, this cannot explain a higher transport in the PIOMAS model compared to BESTMAS, since these two models share the same configuration, except for the resolution and different number of sea ice categories (12 and 8 respectively). Thus, another possibility is that different transports reflect different large-scale forcings of the flow.

Panteleev et al. (2010) applied an inverse model (with ten grid points across the strait) to reconstruct the flow using available data for 1990–1991 and recently calculated the transport through Bering Strait as 0.57 Sv (no stated uncertainty). The data used to reconstruct the circulation were from 12 moorings that were deployed in the Bering Strait and Chukchi Sea from September 1990 to October 1991(Woodgate et al. 2005b). This estimate from Panteleev et al. (2010) tends to agree with the estimates from the BESTMAS and NAME models. In fact, the mean volume transports during the same time period (Sept. 1990–Oct. 1991) were 0.62 (+/−0.03) and 0.59 (+/−0.03) Sv for the BESTMAS and NAME models, respectively.

The model sections presented here show significant vertical and horizontal velocity shear across the strait. This is in contrast to observational results, which show strong coherence of flow and agreement of speeds in the centers of the two channels of the strait, and stronger flow in the ACC. The only currently published sections of observed velocity in the strait are those of Coachman et al. (1975), but as the authors themselves point out, these sections are subject to time aliasing being taken over a period of days. Mooring data shows that the cross-strait velocity variability found outside the ACC on those sections can be explained by temporal variability of the flow.

It seems likely that the variability found in the models is due to edge effects and/or the poor resolution of the real world bathymetry and the exact choice of model section. The lesson to be learned here is that a coarse resolution model cannot be used to study the details of features at the same resolution as the model (e.g. the ACC width of ~10 km). It must also be remembered however, that the observational transports presented here are based on an assumption of homogeneity of flow at all locations in the strait. This is being tested currently by an increased mooring effort in the strait region. Preliminary results suggest this assumption to be reasonably sound outside the ACC region, but more analysis remains to be done.

It seems inevitable that the seasonally-intensified ACC volume transport is not accounted for in models due to spatial resolution limitations. In order to resolve the ACC, models with higher spatial resolution will need to be employed, while maintaining large model domains to obtain proper water mass transformations and

circulations. At the same time, the estimates presented here from observations also lack continuous measurements in the surface layers and near the coast. Although estimates of the contributions from the ACC and stratification have been made by Woodgate et al. (2006, 2010), interannual quantification of the seasonal contribution by the ACC to the overall Bering Strait transport is yet to be computed from either observations or models. The freshwater flux, which has a significant influence on the density structure of the Arctic Ocean (e.g., Aagaard et al. 1985b), would also be better measured if more salinity information could be obtained in the upper layers and especially nearby the coast (see e.g., Woodgate and Aagaard 2005 for discussion). Similarly, for heat flux, it is crucial to get information on the upper layers where maybe 1/3rd of the heat is advected [see Woodgate et al. (2010) who used satellite-derived sea surface temperatures to estimate the contribution from the upper layers]. An international effort is currently underway with eight moorings placed in the Bering Strait region. New information from these moorings will be important for better understanding details of the flow through the strait.

7.6 Summary

While it is encouraging that, in many of the larger-scale models, fluxes of volume, heat and salt are of the right order of magnitude and in interannual terms show correlated variations with observations, there are still significant discrepancies. These have to be considered when using model results to look at the role of Pacific waters in the Arctic. We also see a need for model results with higher spatial resolution in the strait region. The ACC is only in the order of 10 km in width and thus not resolved by global or regional Arctic models with resolutions of 4–40 km (Table 7.1). The implementation of higher-resolution (2 km or less) regional models should improve estimates of the volume, heat and freshwater fluxes in the strait, if the issues of large-scale boundary conditions for such a model can be solved. The challenge is to be able to capture small-scale features, such as the Alaska Coastal Current and mesoscale eddies in the strait itself and its immediate vicinity. The modeling community is working toward that goal to properly represent such features.

Acknowledgments We thank the Department of Energy Earth System Modeling program (J. C. K and W. M.), National Science Foundation Office of Polar Programs (J. C. K, W. M., M. S., and J. Z.), and the Office of Naval Research (J. C. K and W. M.) for support of this research. We also thank the Arctic Ocean Model Intercomparison Project (J. C. K. and W. M.) for travel support and for conference opportunities to present and discuss this research. Support for this work was provided (in part) by NSF grants ARC-0632154, ARC-0855748, and the NOAA-RUSALCA program (R. W.). The mooring data used in this study was collected under funding from ONR, NSF, MMS, AOOS and NOAA-RUSALCA (R. W). At the National Oceanography Centre Southampton (Y.A. and B. d C.) the study was supported by the UK Natural Environment Research Council as a contribution to the Marine Centres' Strategic Research Programme Oceans 2025. The NOCS-ORCA simulations were performed as part of the DRAKKAR collaboration (Barnier et al. 2006). NOCS also acknowledges the use of UK National High Performance Computing Resource. We also thank the editors of this book and two anonymous reviewers for insightful comments, which improved an earlier version of this manuscript.

References

Aagaard K, Carmack EC (1989) The role of sea-ice and other fresh water in the Arctic circulation. J Geophys Res 94:14485–14498

Aagaard K, Roach AT, Schumacher JD (1985a) On the wind-driven variability of the flow through Bering Strait. J Geophys Res 90:7213–7221

Aagaard K, Swift JH, Carmack EC (1985b) Thermohaline circulation in the arctic Mediterranean seas. J Geophys Res 90:4833–4846

Aagaard K, Weingartner TJ, Danielson SL, Woodgate RA, Johnson GC, Whitledge TE (2006) Some controls on flow and salinity in Bering Strait. Geophys Res Lett 33:L19602. doi:10.1029/2006GL026612

Adcroft A, Campin JM (2004) Rescaled height coordinates for accurate representation of free-surface flows in ocean circulation models. Ocean Model 7(3–4):269–284

Adcroft A, Hill C, Marshall J (1997) The representation of topography by shaved cells in a height coordinate model. Mon Weather Rev 125(9):2293–2315

Ahlnäs K, Garrison GR (1984) Satellite and oceanographic observations of the warm coastal current in the Chukchi Sea. Arctic 37:244–254

Arakawa A (1966) Computational design of long-term numerical integration of the equations of fluid motion. J Comput Phys 1:119–143

Barnier B, Madec G, Penduff T, Molines JM, Treguier AM, Le Sommer J, Beckmann A, Biastoch A, Böning C, Dengg J, Derval C, Durand E, Gulev S, Remy E, Talandier C, Theetten S, Maltrud M, McClean J, de Cuevas BA (2006) Impact of partial steps and momentum advection schemes in a global ocean circulation model at eddy permitting resolution. Ocean Dyn 56:543–567. doi:10.1007/s10236-006-0082-1

Brodeau L, Barnier B, Treguier AM, Penduff T, Gulev S (2010) An ERA40-based atmospheric forcing for global ocean circulation models. Ocean Model 31(3–4):88–104. doi:10.1016/j.ocemod.2009.10.005

Clement JL, Cooper LW, Grebmeier JM (2004) Late winter water column and sea ice conditions in the northern Bering Sea. J Geophys Res 109(C3):C03022. doi:10.1029/2003JC002047

Clement JL, Maslowski W, Cooper L, Grebmeier J, Walczowski W (2005) Ocean circulation and exchanges through the northern Bering Sea – 1979–2001 model results. Deep Sea Res II 52:3509–3540. doi:10.1016/j.dsr2.2005.09.010

Coachman LK, Aagaard K (1988) Transports through Bering Strait: annual and interannual variability. J Geophys Res 93:15535–15539

Coachman LK, Aagaard K, Tripp RB (1975) Bering Strait: the regional physical oceanography. University of Washington Press, Seattle

Dai A, Trenberth KE (2002) Estimates of freshwater discharge from continents: latitudinal and seasonal variations. J Hydrometeorol 3:660–687

Daru V, Tenaud C (2004) High order one-step monotonicity-preserving schemes for unsteady compressible flow calculations. J Comput Phys 193(2):563–594, doi: http://dx.doi.org/10.1016/j.jcp.2003.08.023

DRAKKAR Group (2007) Eddy-permitting ocean circulation hindcasts of past decades. CLIVAR Exchanges No 42:12(3):8–10

Dukowicz JK, Smith RD (1994) Implicit free-surface method for the Bryan-Cox-Semtner ocean model. J Geophys Res 99:7791–8014

Fedorova AP, Yankinam AS (1964) The passage of Pacific Ocean water through the Bering Strait into the Chukchi Sea. Deep-Sea Res 11:427–434

Fichefet T, Morales Maqueda MA (1997) Sensitivity of a global sea ice model to the treatment of ice thermodynamics and dynamics. J Geophys Res 102(C6):12609–12646

Flato GM, Hibler WD III (1995) Ridging and strength in modeling the thickness distribution of Arctic sea ice. J Geophys Res 100:18611–18626

Fox-Kemper B, Menemenlis D (2008) Can large eddy simulation techniques improve mesoscale rich ocean models? In: Hecht M, Hasumi H (eds) Ocean modeling in an eddying regime. AGU, Washington, DC

Gill A (1982) Atmosphere–ocean dynamics. Academic Press Inc., Burlington
Goosse H, Campin JM, Fichefet T, Deleersnijder E (1997) Sensitivity of a global ice–ocean model to the Bering Strait throughflow. Clim Dyn 13(5):349–358
Hibler WD III (1979) A dynamic thermodynamic sea ice model. J Phys Oceanogr 9(4):815–846
Hibler WD III (1980) Modeling a variable thickness sea ice cover. Mon Weather Rev 108: 1943–1973
Holland DM (2000) Merged IBCAO/ETOPO5 global topographic data product. National Geophysical Data Center (NGDC), Boulder, CO. http://www.ngdc.noaa.gov/mgg/bathymetry/arctic/ibcaorelatedsites.html. Cited 25 Dec 2000
Jackett DR, McDougall TJ (1995) Minimal adjustment of hydrographic profiles to achieve static stability. J Atmos Oceanic Tech 12(2):381–389
Jakobsson M, Cherkis N, Woodward J, Macnab R, Coakley B (2000) New grid of Arctic bathymetry aids scientists and mapmakers. Eos Trans AGU 81(9):89
Kalnay E et al (1996) The NCEP/NCAR 40-year reanalysis project. Bull Am Meteorol Soc 77:437–471
Kinder TH, Schumacher JD (1981) Circulation over the continental shelf of the Southeastern Bering Sea. In: Hood DW, Calder JA (eds) The eastern Bering Sea shelf: oceanography and resources. University of Washington Press, Seattle
Large WG, Pond S (1981) Open ocean momentum flux measurements in moderate to strong winds. J Phys Ocean 11(3):324–336
Large WG, Pond S (1982) Sensible and latent-heat flux measurements over the ocean. J Phys Ocean 12(5):464–482
Large WG, Yeager SG (2004) Diurnal to decadal global forcing for ocean and sea-ice models: the data sets and flux climatologies. Technical report TN-460+STR, NCAR, 105 pp
Large WG, McWilliams JC, Doney S (1994) Oceanic vertical mixing: a review and a model with a nonlocal boundary layer parameterization. Rev Geophys 32(4):363–403
Leith CE (1996) Stochastic models of chaotic systems. Physica D 98:481–491
Levitus S, Boyer TP, Conkright ME, O'Brian T, Antonov J, Stephens C, Stathopolos L, Johnson D, Gelfeld R (1998) World ocean database 1998, NOAA atlas NESDID 18. US Government Printing Office, Washington, DC
Lique C, Treguier AM, Scheinert M, Penduff T (2009) A model-based study of ice and freshwater transport variability along both sides of Greenland. Clim Dyn 33:685–705. doi:10.1007/s00382-008-0510-7
Losch M, Menemenlis D, Heimbach P, Campin JM, Hill C (2010) On the formulation of sea-ice models. Part 1: effects of different solver implementations and parameterizations. Ocean Model 33:129–144
Madec G (2008) NEMO reference manual, ocean dynamic component: NEMO-OPA. Rep. 27, Note du pôle de modélisation, Institut Pierre Simmon Laplace (IPSL), France. ISSN No. 1288–1619
Madec G, Delecluse P, Imbard M, Levy C (1998) OPA 8.1 ocean general circulation model reference manual. IPSL technical report. Tech Rep. 11, Institut Pierre-Simon Laplace, 91 pp
Marchuk GI, Kagan BA (1989) Dynamics of ocean tides. Kluwer Academic Publishers, Heidelberg
Marshall J, Adcroft A, Hill C, Perelman L, Heisey C (1997) A finite-volume, incompressible Navier–Stokes model for studies of the ocean on parallel computers. J Geophys Res 102(C3):5753–5766
Maslowski W, Marble D, Walczowski W, Schauer U, Clement JL, Semtner AJ (2004) On climatological mass, heat, and salt transports through the Barents Sea and Fram Strait from a pan-Arctic coupled ice-ocean model simulation. J Geophys Res 109:C03032. doi:10.1029/2001JC001039
Melling H (2000) Exchanges of fresh-water through the shallow straits of the North American Arctic. In: Lewis EL et al (eds) The fresh-water budget of the Arctic Ocean. Proceedings of a NATO Advanced Research Workshop, Tallinn Estonia, 27 April–1 May 1998, Kluwer Academic Publishers, Dordrecht, The Netherlands

Menemenlis D, Hill C, Adcroft A, Campin J, Cheng B, Ciotti B, Fukumori I, Heimbach P, Henze C, Koehl A, Lee T, Stammer D, Taft J, Zhang J (2005) NASA supercomputer improves prospects for ocean climate research. Eos Trans AGU 86(9):89, 95–96

Menemenlis D, Campin J, Heimbach P, Hill C, Lee T, Nguyen A, Schodlok M, Zhang H (2008) ECCO2: high resolution global ocean and sea ice data synthesis. Mercat Ocean Q Newsl 31:13–21

Nguyen AT, Menemenlis D, Kwok R (2009) Improved modeling of the Arctic halocline with a subgrid-scale brine rejection parameterization. J Geophys Res 114:C11014. doi:10.1029/2008JC005121

Nguyen AT, Menemenlis D, Kwok R (2011) Arctic ice-ocean simulation with optimized model parameters: approach and assessment. J Geophys Res 116:C04025. doi:10.1029/2010JC006573

Onogi K, Tsutsui J, Koide H, Sakamoto M, Kobayashi S, Hatsushika H, Matsumoto T, Yamazaki N, Kamahori H, Takahashi K, Kadokura S, Wada K, Kato K, Oyama R, Ose NMT, Taira R (2007) The jra-25 reanalysis. J Meteorol Soc Jpn 85(3):369–432

Panteleev GG, Nechaev D, Proshutinsky AY, Woodgate R, Zhang J (2010) Reconstruction and analysis of the Chukchi Sea circulation in 1990–1991. J Geophys Res 115:C08023. doi:10.1029/2009JC005453

Paquette RG, Bourke RH (1974) Observations on the coastal current of arctic Alaska. J Mar Res 32:195–207

Payne RE (1972) Albedo at the sea surface. J Atmos Sci 29:959–970

Penduff T, Le Sommer J, Barnier B, Treguier AM, Molines JM, Madec G (2007) Influence of numerical schemes on current-topography interactions in 1/4° global ocean simulations. Ocean Sci 3:509–524

Prange M, Lohmann G (2004) Variable freshwater input to the Arctic Ocean during the Holocene: implications for large-scale ocean-sea ice dynamics as simulated by a circulation model. In: Fischer H et al (eds) The KIHZ project: towards a synthesis of Holocene proxy data and climate models. Springer, New York

Prather MC (1986) Numerical advection by conservation of second-order moments. J Geophys Res 91:6671–6681

Roach AT, Aagaard K, Pease CH, Salo SA, Weingartner T, Pavlov V, Kulakov M (1995) Direct measurements of transport and water properties through the Bering Strait. J Geophys Res 100:18443–18457

Royer TC (1981) Baroclinic transport in the Gulf of Alaska, part II. A freshwater driven coast current. J Mar Res 39:251–266

Semtner AJ (1976) A model for the thermodynamic growth of sea ice in numerical investigation of climate. J Phys Oceanogr 6:376–389

Shimada K, Kamoshida T, Itoh M, Nishino S, Carmack E, McLaughlin F, Zimmermann S, Proshutinsky A (2006) Pacific Ocean inflow: influence on catastrophic reduction of sea ice cover in the Arctic Ocean. Geophys Res Lett 33:L08605. doi:10.1029/2005GL025624

Smith WHF, Sandwell DT (1997) Global sea floor topography from satellite altimetry and ship depth soundings. Science 277(5334):1956–1962

Smith RD, Dukowicz JK, Malone RC (1992) Parallel ocean general circulation modeling. Physica D 60:38–61

Steele M, Morley R, Ermold W (2001) PHC: a global ocean hydrography with a high quality Arctic Ocean. J Clim 14(9):2079–2087

Thorndike AS, Rothrock DA, Maykut GA, Colony R (1975) The thickness distribution of sea ice. J Geophys Res 80:4501–4513

Timmermann R, Goose H, Madec G, Fichefet T, Ethe C, Duliere V (2005) On the representation of high latitude processes in the ORCA-LIM global coupled sea ice-ocean model. Ocean Model 8:175–201

Weingartner TJ, Danielson S, Sasaki Y, Pavlov V, Kulakov M (1999) The Siberian Coastal Current: a wind- and buoyancy-forced Arctic coastal current. J Geophys Res 104:29697–29713. doi:10.1029/1999JC900161

Woodgate RA, Aagaard K (2005) Revising the Bering Strait freshwater flux into the Arctic Ocean. Geophys Res Lett 32:L02602. doi:10.1029/2004GL021747

Woodgate RA, Aagaard K, Weingartner TJ (2005a) Monthly temperature, salinity, and transport variability of the Bering Strait throughflow. Geophys Res Lett 32:L04601. doi:10.1029/2004GL021880

Woodgate RA, Aagaard K, Weingartner TJ (2005b) A year in the physical oceanography of the Chukchi Sea: moored measurements from autumn 1990–1991. Deep Sea Res II 52:3116–3149. doi:10.1016/j.dsr2.2005.10.016

Woodgate RA, Aagaard K, Weingartner TJ (2006) Interannual changes in the Bering Strait fluxes of volume, heat and freshwater between 1991 and 2004. Geophys Res Lett 33:L15609. doi:10.1029/2006GL026931

Woodgate RA, Aagaard K, Weingartner TJ (2007) First steps in calibrating the Bering Strait throughflow: preliminary study of how measurements at a proposed climate site (A3) compare to measurements within the two channels of the strait (A1 and A2). 20 pp, University of Washington, Seattle, WA

Woodgate RA, Weingartner TJ, Lindsay RW (2010) The 2007 Bering Strait oceanic heat flux and anomalous Arctic sea-ice retreat. Geophys Res Lett 37:L01602. doi:10.1029/2009GL041621

Zhang J (2005) Warming of the arctic ice-ocean system is faster than the global average since the 1960s. Geophys Res Lett 32:L19602. doi:10.1029/2005GL024216

Zhang J, Hibler WD (1997) On an efficient numerical method for modeling sea ice dynamics. J Geophys Res 102:8691–8702

Zhang J, Rothrock DA (2001) A thickness and enthalpy distribution sea-ice model. J Phys Oceanogr 31:2986–3001

Zhang J, Rothrock DA (2003) Modeling global sea ice with a thickness and enthalpy distribution model in generalized curvilinear coordinates. Mon Weather Rev 131:681–697

Zhang J, Rothrock DA (2005) The effect of sea-ice rheology in numerical investigations of climate. J Geophys Res 110:C08014. doi:10.1029/2004JC002599

Zhang J, Steele M, Lindsay RW, Schweiger A, Morison J (2008) Ensemble one-year predictions of arctic sea ice for the spring and summer of 2008. Geophys Res Lett 35:L08502. doi:10.1029/2008GL033244

Zhang J, Woodgate R, Moritz R (2010) Sea ice response to atmospheric and oceanic forcing in the Bering Sea. J Phys Oceanogr 40:1729–1747. doi:10.1175/2010JPO4323.1